Seismic evidence of gas hydrates, multiple BSRs and fluid flow offshore Tumbes Basin, Peru

Constance Auguy, Gérôme Calvès, Ysabel Calderon, Stéphane Brusset

Seismic evidence of gas hydrates, multiple BSRs and fluid flow offshore Tumbes Basin – Peru.

Constance Auguy [1], Gérôme Calvès [1*], Ysabel Calderon [1,2], Stéphane Brusset [1]

[1] Université Toulouse 3, GET-OMP, 14 Avenue Edouard Belin, 31400, Toulouse, France

(*corresponding author, gerome.calves@get.omp.eu, phone: +33561332598, fax: +33561332560)

[2] PeruPetro, Lima, Peru.

ABSTRACT (247 words)

Identification of a previously undocumented hydrate system in the Tumbes Basin, localized off the north Peruvian margin at latitude of 3°20' – 4°10'S, allows us to better understand gas hydrates of convergent margins, and complement the 36 hydrate sites already identified around the Pacific Ocean. Using a combined 2D-3D seismic dataset, we present a detailed analysis of seismic amplitude anomalies related to the presence of gas hydrates and/or free gas in sediments. Our observations identify the occurrence of a widespread Bottom Simulating Reflector (BSR), under which we observed, at several sites, the succession of one or two BSR-type reflections of variable amplitude, and vertical acoustic discontinuities associated with fluid flow and gas chimneys. We conclude that the uppermost BSR marks the current base of the hydrate stability field, for a gas composition comprised between 96% methane and 4% of ethane, propane and pure methane. Three hypotheses are developed to explain the nature of the multiple BSRs. They may refer to the base of hydrates of different gas composition, a remnant of an older BSR in the process of dispersion/dissociation or a diagenetically induced permeability barrier formed when the active BSR existed stably at that level for an extended period. The multiple BSRs have been interpreted as three events of steady state in the pressure and temperature conditions. They might be produced by climatic episodes since the last glaciation associated with tectonic activity, essentially tectonic subsidence, one of the main parameters that control the evolution of the Tumbes Basin.

Keywords

Gas hydrates, Bottom Simulating Reflector, multiple BSRs, seismic chimneys, Tumbes, Peru.

Introduction

Natural gas hydrates have gained international attention over the last few decades for energy, safety and environmental reasons (Kvenvolden, 1993; Milkov, 2004; Sultan *et al.*, 2004). Because they are thermodynamic products, they can be extremely useful to indirectly estimate heat flow of continental margins (Yamamo *et al.*, 1982), and can provide valuable information on environmental and/or tectonic evolution of a sedimentary basin.

Gas hydrates are formed by a lattice of water molecules held together by hydrogen bonding, and stabilized by the inclusion of a guest molecule, typically low molecular weight gas (Ballard and Sloan, 2002). Natural gas molecules trapped in hydrate consist mainly of methane, but other higher and non-hydrocarbons, such as nitrogen, hydrogen sulfide or carbon dioxide, can also form hydrates. To form, gas hydrates need high pressure, low temperature, and the right amount of water and gas (Kvenvolden, 1993), conditions commonly found in oceanic sediments along continental margins, at water depths greater than 400 m. The field of hydrate stability, called the Gas Hydrate Stability Zone (GHSZ), comprises the first few hundred meters of the sedimentary section. It is largely controlled by pressure and temperature conditions, and is limited in depth due to increasing temperature from the local geothermal gradient.

In seismic reflection section, a common indicator of submarine gas hydrates is a Bottom-Simulating Reflector (BSR) (Shipley *et al.*, 1979), although its absence does not necessarily mean absence of hydrates in sediments (Vanneste *et al.*, 2001). A hydrate-related BSR mimics the seafloor topography and crosscuts the sedimentary strata as it follows the GHSZ. It is characterized by a strong negative impedance contrast due to high-velocity sediments containing hydrates above the base of the hydrate stability field and lower-velocity sediments containing free gas beneath it (Field and Kvenvolden, 1985). If the gas composition is known, the in situ temperature at the BSR can be estimated from the depth of this reflector.

When a hydrate system is not in thermodynamic equilibrium, the position of the BSR is expected to change. Multiple BSR-type reflections, subparallel to the seafloor but at different sub-bottom depths, have been observed in both active and passive margins, as the Storegga Slide area on the Norwegian margin (Posewang and Mienert, 1999; Andreassen et al.,2000)), the upper slope of the SE Nankai margin (Foucher *et al.*, 2002), in the Yaquina and Trujillo Basins off Peru (Hübscher and Kukowski, 2003; Herbozo *et al.*,

2013), at Hydrate Ridge on Cascadia margin (Bangs *et al.*, 2005), in the Danube deep-sea fan on the NW Black Sea margin (Popescu *et al.*, 2006), or in the Mohican Channel area on the central Scotian Slope (Mosher, 2008). The origin of these multiple reflectors is not well understood, and several interpretations have been suggested, i.e. residual BSR in the process of dispersing, layers of hydrates of different gas composition, or diagenetic reaction.

Along South American continental margins, numerous accumulations of gas hydrates are known and have been described (Kvenvolden and Kastner, 1990; Brown *et al.*, 1996; Pecher *et al.*, 2001; Hubscher and Kukowski, 2003; Rodrigo *et al.*, 2009). Off Peru, during Ocean Drilling Program (ODP) Leg 112, gas hydrates were identified in water depth greater than 3000 m, within core drillings, and on seismic profiles crossing the Yaquina and Lima forearc Basins (sites 682, 685, and 688) (von Huene *et al.*, 1987) (Figure 1A). The occurrence of BSRs in these basins was interpreted to reflect a history of vertical tectonism, sedimentation, and carbon concentrations in sediments (von Huene and Pecher, 1999). Off margin north of Peru, no data were available until recent 2D-3D seismic reflection data acquisition in the Tumbes Basin, which allowed the identification of a new hydrate province (Figure 1B).

The purpose of this study is to (1) document the hydrates in the Tumbes Basin (2) describe associated fluid seeps (3) estimate the thermal regime and (4) discuss the influence of climatic changes and tectonic factors related to the evolution of the margin that help generate multiple BSRs.

2. Geological framework

The Tumbes Basin is a particular type of forearc basin which evolves in response to subduction dynamics of the Nazca plate beneath the South America plate. The study area, located offshore northern Peru between 3°20 and 4°10S, consists of a several-kilometer-thick accumulation of Oligocene to Quaternary sediment characterized by normal faulting (Figure 1C). It is delineated by three major N-S-trending normal and low-angle gravity-driven fault systems. These gravitational tectonic features have generated rollover anticlines and rotated fault blocks during Pliocene-Pleistocene times. To the west, an east-dipping normal fault bounds the eastern flank of Banco Peru, a flat shallow-depth seafloor high located 30-50 km seaward from the coast, which bounds the extension of the basin to the west. The southern limit of the basin occurs near 4°S as the triple junction between these two major fault systems and a south-dipping listric normal fault branched onto the Talara detachment, which extends to the Peru-

Chile trench axis at ~5°S (Bourgois *et al.*, 2007). The presence of multiple reservoirs, giant oil accumulation in the onshore fields of the Talara Basin and different hydrocarbon occurrences in the eastern shallow-depth Tumbes Basin (Deckelman *et al.*, 2005), makes the study area a promising region for hydrocarbon exploration.

3. Data and methods

The seismic reflection dataset was acquired over exploration block Z-38, in water depths ranging from 110 m to 2765 m, offshore Tumbes Basin (Figure 1B). The 2D mutli-channel seismic data acquired in 2009 has a total survey length of about 2393 km. The dataset has a sampling rate of 2 ms. The frequency content ranges between 10–70 Hz and the 2D grid spacing ranges from 1 to 6 km. Dominant frequencies around 45 Hz for the shallow subsurface provide a theoretical vertical resolution (λ/4) of ~10 m (P-wave velocity in sediments of 1800 m/s). The 3D seismic dataset, acquired in 2010, covers an area of 1500 km^2. It has a sampling rate of 4 ms. The 3D grid is subdivided into inline and crossline directions, spaced at 25 m and 12.5 m respectively. The frequency of the seismic signal in the shallow subsurface ranges between 5 and 90 Hz with a dominant frequency around 45–55 Hz. Assuming a velocity of 1800 m/s, the theoretical vertical resolution (λ/4) is ~9 m.

The seismic data have been interpreted using standard seismic stratigraphic techniques (Mitchum *et al.*, 1977), based on reflection terminations and seismic facies reflection characteristics. Geometric seismic attributes, such as similarity, have been used to enhance recognition of coherent events and emphasize discontinuities such as faults and stratigraphic surfaces. Using these techniques, a framework of four interpreted seismic horizons (seafloor, H1, H2 and H3; Figure 2A) has been used in the Mancora Basin, a sub-basin of the Tumbes Basin (red dashed box Figure 1B), in order to obtain accurate and detailed information on amplitude anomalies, depositional elements, structural patterns, direct hydrocarbon indicators (DHI), and sediment remobilization or fluid flow features (Calvès *et al.*, 2008).

As hydrates are only stable in a very limited range of temperatures and pressures (Yamano *et al.*, 1982; Sloan, 1998), the occurrence of BSRs related to methane hydrates in the shallow subsurface allows us to estimate the thermal regime. This estimation is based on the assumption that the BSR is related to the base of the GHSZ. We have used information from seismic reflection surveys, seabed temperature from World Ocean Database (http://www.nodc.noaa.gov/OC5/WOD09/pr_wod09.html–2009) and Sloan's

(1998) phase boundary diagram for pure methane and 3.5 wt% seawater. The workflow consists of the following steps (e.g. Calvès *et al.*, 2010): (1) picking of seabed and regional BSR horizons, (2) conversion from two-way time (TWT) to depth, based on a P-wave velocity of 1475 m/s in seawater and 1800 m/s in sediments, (3) conversion from BSR depth to temperature using a phase boundary diagram, (4) determination of the thermal gradient computed by dividing the temperature difference between the seabed and the BSR by the subbottom depth.

4. Results

4.1. Seismic evidence of multiple BSRs: characteristics and distribution

Analysis of seismic reflection profiles revealed the presence of numerous BSRs in water depths of 470-2410 m. We identified an extensive BSR (Figure 1D and upper BSR, Figure 3) under which we observed, at several sites, the succession of one or two BSR-type reflections at different depths (intermediate and lower BSRs, Figure 3). All of them mimic the seafloor topography, cross-cutting stratigraphic horizons, and display reversed polarity relative to the seafloor reflection. Below these multiple BSRs, enhanced reflections are commonly observed (e.g. HAA: Calvès *et al.*, 2008; Figure 3A). This association of BSRs with reversed apparent polarity and the abrupt termination of enhanced reflections against them indicate the occurrence of gas hydrates overlying free gas accumulations. Other anomalous amplitude reflections are observed in the shallow subsurface, and identified as Direct Hydrocarbon Indicators (DHIs) (Figure 2B). DHIs are particularly present in the SW part of the 3D seismic block in the intra-slope Mancora Basin (Figure 2A), where they occur as local increases or decreases in reflection amplitudes (called bright spots/flat spots or dim outs respectively), phase reversals along particular sedimentary reflections and BSRs, and columnar disturbances linked to fluid seeps, which are interpreted as seismic chimneys.

Among the multiple BSRs identified, the upper one (Figure 1D and upper BSR, Figure 3) is the longest and can be followed over distances of up to 15 km without interruption. The isochore of the interval from the seabed to the upper BSR (Figure 4A) shows a variation in thickness from 170 to 560 m, and increases with increasing water depth, i.e. with pressure; it is controlled by the gas hydrate stability conditions. As observed in other hydrate provinces, the upper BSR undergoes important amplitude variations depending on which structural features or geological elements it intersects (Ashi *et al.*, 2002; Lin *et al.*, 2008). Contrary to observations done in the Yaquina Basin further south by Hübscher and Kukowski (2003), the

upper BSR is most easily recognized where it cross-cuts sedimentary strata. It displays strong amplitude in anticline structures, or cross-cutting inclined stratal reflections on structural ridges, and is weaker in synclinal structures, slope basins, or sub-marine canyons. In the intra-slope Mancora Basin, the upper BSR cross-cuts parallel stratified sediments with a small angle (Figure 2A). Its reflection is superimposed on the underlying sedimentary reflections, which makes it difficult to follow. On some seismic profiles, that intersection can be seen and is characterized by local decreases in amplitude and polarity changes of the strong sedimentary reflections intersected (dim out and phase reversal – Figures 2A and 2B).

Intermediate BSRs are observed at depths ranging from 36 to 72 m (40 to 80 ms TWT) below the upper BSR. They appear as negative polarity reflections or an upper limit of enhanced reflections, mimicking the seafloor topography (Figures 3A and 3B). As with the upper BSR, they have a water-depth dependence (Figure 4B), but are much more discontinuous. They occur locally as patches of high amplitude reflections of 50 to 250 m (Figure 4C), or as reflection segments of 1000 to 2600 m (Figure 4D), and are generally located in zones strongly affected by normal faults.

Lower BSRs are observed at depths ranging from 115 to 190 m (130 to 210 ms TWT) below the upper BSR. They appear as discontinuous reflection segments of 200 to 2800 m long, display reversed polarity and are, in most seismic profiles where they occur, the BSRs showing the strongest amplitude values. They are present within different structural and sedimentological settings, from a buried structural high with near-vertical stratal reflections (Figures 3A and 4C), to stratigraphic layers sub-parallel to the seabed and affected by normal faults (Figure 3B).

A particular type of HAA, which have the same negative polarity as a hydrate-related BSR but are affected by a fault system that shifts them downward, are observed in the Mancora Basin (Figures 2A and 3C). Approximately parallel to the seabed, they extend semi-continuously over the intra-slope basin, cross-cutting the background inclined sedimentary reflections. Their depth below seafloor varies from 480 to 810 m (530 ms to 810 ms TWT) for water depths of 950–1030 m respectively. In seismic profiles oriented NW-SE, they appear as flat spot of over 2000 m long (yellow triangle, Figure 2A), while in seismic profiles oriented perpendicularly (SW-NE), they appear as high reflectivity segments shifted down between sub-parallel normal faults (right profile, Figure 3C). The extension of these HAA is difficult to

visualize due to their location at the boundary between the 3D block and the 2D seismic data, but they seem to fit with the lower BSR observed in the 2D seismic profile (NW-SE section– Figure 3C).

4.2. Distribution of fluid seeps

In the Mancora Basin, within ~100 km^2 imaged by the 3D seismic reflection (Figure 5), we have identified a series of pockmarks/mounds that consist of patches of HAA on the seabed and 10-15 m deep/high on seismic profiles. These features are the expressions of focused fluid flow activity on the seabed (Judd and Hovland, 2009; Hustoft *et al.*, 2009). Depending on their morphology, we defined two categories of pockmarks: the circular or elliptic ones, typically measuring from 40 to 350 m in diameter, and the elongated ones, which have one axis that is much longer than the other, up to 500 m (e.g. chimney α: 85 m wide, and 515 m long, Figures 5 and 6). Underlying the pockmarks/mounds field lies a corresponding series of vertical seismic chimneys, i.e. the acoustic imprint of fluid migration. Time-structure/similarity attribute maps of three paleo-surfaces illustrates the subsurface expression of the fluid-escape chimneys in plan form (H1, H2, H3, Figures 2A and 6). The maps show that chimneys are represented by circular and elongated well-exposed anomalies, and reveal a preferred direction of the elongated chimneys, with the longest axis perpendicular to the faulting. This preferred direction remains commonly constant with depth (Figure 6). In seismic reflection sections, the chimneys appear as columnar zones of low coherence and reduced reflectivity, where surrounding strata can be both truncated or flexed upward at their flanks. Of 48 seismic chimneys identified, one fifth are buried chimneys ending at different stratigraphic levels, generally with a patch of high amplitude reflections or intra-sedimentary doming, i.e. deflected upward reflections stopped into the sediment column (e.g. chimneys γ and δ, Figure 5). A typical chimney has a root zone that in the seismic data appears to originate below the strong stratigraphic clustering that occurs throughout the intra-slope basin, between 315 to 540 m (350 to 600 ms TWT) subsurface depths (Figure 2A). In some areas attenuation and scattering of the seismic signal suggest the presence of free gas accumulation.

4.3. Estimated geothermal gradient from BSR depth

Variations in the thermal regime of sedimentary basins can be a good indicator of tectonic features and/or fluid migration through the sedimentary column. In the undrilled part of the Tumbes Basin, the geothermal gradient is computed using the inferred temperature at the BSR (Yamano *et al.*, 1982;

Hyndman *et al.*, 1992), assuming hydrostatic pressure, and a gas composition of pure methane, which seems a good approximation for the Peru margin (Pecher *et al.*, 2001). As temperature is available only at the seabed (World Ocean Database, 2009), the estimated thermal gradient values are used only for qualitative assessments. Using the methodology described above, the seafloor (water depth ranging from 110 to 2765 m), and the BSR (depth below seafloor ranging from 171 to 558 m) are mapped in detail from the 2D and 3D seismic dataset (Figures 7A and 7B). Temperature at the BSR is estimated from pressure-temperature curves for seawater-methane hydrate stability based on experimental data, and the derived geothermal gradient is mapped and extrapolated across the mapped BSR (Figure 7C). The average value obtained, 26°C/km, is consistent with the regional thermal regime trend. In the Yaquina and Lima Basins, Kvenvolden and Kastner (1990) obtained values of 40-50°C/km at water depths greater than 3000 m, which fit with our estimation of a thermal gradient close to 40°C/km at a water depth of ~3000 m.

In order to assess potential uncertainties due to gas composition, we use the seawater approximation with variable mixtures of methane, ethane, and propane, i.e. 100% methane, mixte (96% methane, 3% ethane, 1% propane), and thermogenic (90% methane, 7% ethane, 3% propane). We then use an average geothermal gradient of 25-40°C/km for the study area (Figure 8), to estimate the approximate expected depth of the hydrate stability zone, and therefore the potential depth of the BSR below the seafloor. Hydrates are predicted to be stable in sediment from 125 to 780 m below seafloor, based on a hydrate stability field for a three variable mixture of gas and assuming a 25-40°C/km geothermal gradient and water depths of 765, 950, 1115 and 1330 m. Our results are summarized in Table 1.

5. Discussion

5.1. Nature of the BSRs

Although direct analyses of hydrate composition are not available in the Tumbes and Mancora Basins, we interpret the upper BSR as the active BSR, in part because it is the BSR that shows the greatest continuity and that is not affected by faults. Moreover, the data presented reveal that the upper BSR corresponds to the present-day position of the base of the hydrate stability field, estimated from pressure-temperature conditions exerted at seafloor and in sediment, and a gas composition comprised between 96% methane and 4% of ethane, propane and pure methane. Locally, CO_2 may be present as well as thermogenic gases, according to the seawater-hydrate stability curves. These results seem consistent

with previous reported analyses done in the Piedra Redonda and Corvina gas wells, located eastward of block Z-38 in the shallow depth Tumbes Basin, which show a gas composition with near 98% methane and 2% of ethane, propane and CO_2 (Basin Evaluations Group Exploration Department, 2005).

For the other deeper BSR-type reflectors, which we interpret as possible hydrate-related BSRs, we have three hypotheses:

(1) Intermediate and lower BSRs could represent the base of hydrates formed from a mixture of gases. Hydrates with mixed compositions of methane and heavier natural gas components such as ethane, propane or carbon dioxide, will cause an increase in depth of the base of the GHSZ, due to the displacement of the phase boundary to higher temperature-pressure values (Sloan, 1998). In the Tumbes Basin, we calculated that intermediate and lower BSRs are all within the stability range of hydrates for variable mixtures of methane, ethane and propane (with less than 10% of the heavier hydrocarbon gases) (Table 1). Conversely, in the intra-slope Mancora Basin, although both fluid-flow features and gas hydrate accumulations may indicate the presence of a deep thermogenic gas source (Heggland, 1998), the HAA occur at depths where the ambient temperature is too high for the hydrate to be stable, even in the presence of more complex gas/fluid components (section SW-NE – Figure 3C). Our results may support the hypothesis that intermediate and lower BSRs mark the base of hydrates of different gas compositions, although no current data allows us to confirm this hypothesis.

(2) In response to variations in pressure and temperature conditions exerted on the GHSZ, vertical displacement of the BSR is expected. Intermediate and lower BSRs could be interpreted as a remnant of an older BSR that is in the process of dispersing, after a pressure drop and/or a temperature increase (e.g. von Huene and Pecher, 1999; Foucher *et al.*, 2002, Bangs *et al.*, 2005). This hypothesis supposes that the amount of free gas is still high enough that the reflectivity of the old BSR persists. Foucher *et al.* (2002) estimated the duration of persistence of a diffusing gas layer at several thousand years, with a maximum of the order of 10 000 yr. We suggest three thermodynamic stability periods to form the lower, intermediate, and upper BSRs, during the last 10 000 yr as required by the estimated short duration of the BSR's reflectivity.

(3) We suggest that multiple BSRs may represent a permeability barrier (e.g. diagenetically induced) formed when the active BSR existed stably at that level for an extended period. The permeability barrier

would allow the trapping and accumulation of free gas, which would be expressed in seismic data as a negative reflection, and as a level at which enhanced reflections would terminate. We excluded here the possibility of a diagenesis-related BSR resulting from the phase transitions between opal-A, opal-CT/-C, and microcrystalline quartz, which displays the same polarity as the seafloor reflection, opposite to that of a hydrate-related BSR (Berndt *et al.*, 2004).

5.2. Mechanisms at the origin of BSR migration

Multiple BSRs that would correspond to a previously deeper phase boundary BSR, either in the process of dispersing or diagenetically induced, have to readjust their position to current pressure and temperature conditions. We will discuss the main mechanisms that could generate vertical movement of the base of the GHSZ to explain their origin. In the Tumbes basin, these mechanisms are associated with eustatic, tectonics and sedimentary processes, the main parameters that control the evolution of the basin through time. We will not further develop the hypothesis of hydrates formed from a gas mixture, which would need borehole data to be substantiated.

Since the last glacial maximum, the eustatic sea level increased by 125 +/- 5 m from ~15 to 7 ka and stayed roughly constant from 7 ka until present time (Fleming *et al.*, 1998), and bottom water temperature was estimated 1.5°C cooler than today (data from deep-sea core V 19–30; 3091 m water depth, Koutavas, *et al.*, 2006) in the Equatorial Pacific Ocean (Chappell and Shackleton, 1986; Waelbroeck *et al.*, 2002). Pressure and temperature changes affect the BSR with different timing. The pressure, which increased nearly uniformly during 10 ka, is transferred immediately to the depth of the BSR. Conversely, the thermal pulse associated with rising bottom-water temperatures propagates gradually, from the seafloor down to the BSR depth, following the laws of thermal conduction (e.g. on the upper slope of the eastern Nankai margin, Foucher *et al.* (2002) estimated a time delay of 4700 yr before the thermal pulse would affect local temperature conditions at 200 m sub-bottom depth, for a thermal diffusivity of the sediments of 3×10–7 m²/s,). In order to determine the possible depth of the paleo-BSR that could correspond to the last glacial pressure-temperature conditions, we computed the depth of the BSR for a seafloor temperature 1.5°C lower than today, assuming sea-level lowstand of ~120 m for pure methane hydrates and a geothermal gradient of ~30°C/km (Figure 9). Our results show that multiple BSRs can be locally interpreted as the result of different stable climatic episodes, with temperature between glacial

values and the present-day conditions (for a mixte or thermogenic gas composition, the interval between the two theoretical BRSs increases and includes the lower BSRs, see Table 1).. Nevertheless, the importance of faulting and associated shift of the multiple BSRs lead us to suspect that tectonic subsidence/uplift could play a major role in addition to sea level rise and thermal pulse.

In the Tumbes Basin, and more widely along the Peru margin, the presence or absence of a BSR is largely controlled by tectonism and sedimentation (e.g. von Huene and Pecher, 1999). The Tumbes Basin is defined as a complex forearc basin. It is controlled by detachment tectonics, the Tumbes and Zorritos detachments, which accommodate the main subsidence phase that has been occuring since the late Pliocene-Pleistocene until present time (Witt and Bourgois, 2010). We hypothesize that tectonic subsidence is the main controlling factor for multiple BSRs generation. The intra-slope Mancora Basin shows a nice example of such activity. Indeed, we suggest that the HAA shifted down observed in this sub-basin are related to a paleo BSR, probably the same as that called 'lower BSR' observed in profile 3C. The intra-slope Mancora Basin is located at the complex triple junction between the Tumbes detachment, the normal fault bounding the eastern flank of Banco Peru, and the Talara detachment. It is controlled by a major seaward-dipping listric fault (i.e., the Talara detachment, Witt and Bourgois, 2010), which controls the subsidence of the intra-slope basin, and displaced the seafloor producing a 220 m-high scarp. The listric fault and the growth of antithetic faults are at the origin of the shift of the paleo-BSR (Figures 10A and 10B). Thereafter, sediment deposition thickens towards the listric fault, increasing pressure and temperature, causing the dissociation of the deepest segments of the BSR. This step probably coincides with the first chimneys' appearance in the intra-slope basin and the reactivation of antithetic faults which facilitated fluid migration (Figure 10C). The last sediment depositions are flat lying and are not cut by the antithetic faults, which suggests a reduced activity of the listric fault, and a period of relatively stable P-T conditions allowing the formation of the upper BSR (Figure 10D). The preservation of the reflectivity of the old BSR supposes that amount of free gas remains stable enough to prevent it from dispersing quickly by diffusion (Bangs et al., 2005). Little or no fluid advection is required to explain the retention of the lower BSRs. The areas where intermediate BSRs occur have in common a structural architecture characterized by high concentration of normal faults. We suggest that the fracture pathways may contribute to disperse BSRs faster due to upward migration of warm fluid migration which partially destroys the multiple BSRs

(Tréhu *et al.*, 2006). Moreover, lower BSRs in these zones are usually very faint or absent, which is consistent with this hypothesis.

5.3. Plumbing system and BSR

The plumbing system of the Tumbes-Mancora Basin for its shallow portion is complex with faults outcropping at the seafloor surface and buried to outcropping gas chimneys/pipes and pockmarks (Figures 1B, 2, 5 and 6). The inferred evidence from the BSRs for hydrate bearing sediments means that the fluids that circulate/migrates within these basins can be trapped due to high pressure and low temperature at seafloor. The buried features such as gas chimneys show vertical migration rather that stratal migration from deeper sourced fluids to the shallow subsurface. This is well depicted by the faults mapped within the 3D area covered of the Mancora Basin (Figures 5 and 6). Figures 5 and 6 illustrate the location of vertical discontinuities such as gas chimneys that originates from various depth levels. They are not all spatially linked to the presence of the BSR. They illustrate various levels of source/root zones such as compiled by Cartwright and Santamarina (2015), with the source being above, at and below the BSR in various hydrates provinces. The relation between pipes/gas chimneys and hydrate is not yet fully understood (e.g. Paull *et al*., 2008). The highly heterogeneous occurrence of the root zones of pipes/gas chimneys around the GHSZ and BSR might express the complex variations of mechanism related to fracture induced processes due to upward migration of free gas and hydrate nucleation and/or dissociation related to physical/chemical processes.

6. Conclusions

Seismic data acquired in the Tumbes Basin have revealed the occurrence of an extended active hydrate-related BSR, and multiple BSRs observed at different sub-bottom depths below, comprising a lower BSR of high reflectivity and several soft intermediate BSRs localized within the interval between the active and lower BSR. We have focused our attention on the multiple BSRs which may represent segments of residual BSRs in the process of dispersing, or related to a permeability barrier left behind after an upward displacement of the base of the GHSZ. They have been interpreted as three events of steady state in the pressure and temperature conditions, produced by climatic episodes since the last glaciation associated with tectonic activities, essentially tectonic subsidence regarding the Tumbes-Mancora Basins. This paper document hydrates using seismic data only. Further investigations must be

conducted by developing geophysical tools, and drilling cores in hydrate zones, to better understand the distribution of gas hydrates in sediment and the nature of the multiple BSRs in the area.

Acknowledgements

We thank PeruPetro for providing access to the seismic data, IHS-KINGDOM and dGB-OpendTect for academic software donation. An earlier version of this manuscript has been critically and constructively reviewed by T. Alves, M. De Batist, M. Huuse and C. Série. We are grateful to the anonymous referee, Philippe Schnürle and the editor Wu-Cheng Chi, who provided constructive suggestions.

Conflict of Interest

The authors declare that they have no conflict of interest.

References

Andreassen K., Mienert J., Bryn P., Singh S.C. (2000) A double gas-hydrate related bottom-simulating reflector at the Norwegian continental margin. Ann. N.Y. Acad. Sci., 912, 126–135. doi:10.1111/j.1749-6632.2000.tb06766.x

Ashi J., Tokuyama H., Taira A. (2002) Distribution of methane hydrate BSRs and its implication for the prism growth in the Nankai Trough. Marine Geology, 187, 177–191. doi:10.1016/S0025-3227(02)00265-7

Ballard A. L., Sloan E. D. (2002) The next generation of hydrate prediction: I. Hydrate standard states and incorporation of spectroscopy. Fluid Phase Equilibria, 194, 371–383. doi:10.1016/S0378-3812(01)00697-5

Bangs N. L. B., Musgrave R. J., Tréhu A. M. (2005) Upward shifts in the southern Hydrate Ridge gas hydrate stability zone following postglacial warming, offshore Oregon. Journal of Geophysical Research, 110, B03102. doi:10.1029/2004JB003293

Berndt C., Bünz S., Clayton T., Mienert J., Saunders M. (2004) Seismic character of bottom-simulating reflections: examples from the mid-Norwegian margin. Mar. Pet. Geol., 21, 723–733. doi:10.1016/j.marpetgeo.2004.02.003

Bourgois J., Bigot-Cormier F., Bourles D., Braucher R., Dauteuil O., Witt C., Michaud F. (2007) Tectonic record of strain buildup and abrupt coseismic stress release across the northwestern Peru coastal plain,

362 shelf, and continental slope during the past 200 kyr. Journal of Geophysical Research: Solid Earth, 112,
363 B04104, doi: 10.1029/2006JB004491.
364 Brown K. M., Bangs N. L., Froelich P. N., Kvenvolden K. A. (1996) The nature, distribution, and origin of
365 gas hydrate in the Chile Triple Junction region. Earth and Planetary Science Letters 139, 471-483. doi:
366 10.1016/0012-821X(95)00243-6
367 Calvès G., M. Huuse, A. Schwab, and P. Clift (2008) Three-dimensional seismic analysis of high-
368 amplitude anomalies in the shallow subsurface of the Northern Indus Fan: Sedimentary and/or fluid
369 origin, J. Geophys. Res., 113, B11103, doi: 10.1029/2008JB005666.
370 Calvès G., Schwab A. M., Huuse M., Clift P. D., Inam A. (2010) Thermal regime of the northwest Indian
371 rifted margin – Comparison with predictions. Marine and Petroleum Geology, 27, 1133–1147. doi:
372 10.1016/j.marpetgeo.2010.02.010
373 Cartwright J., Santamarina C. (2015), Seismic characteristics of fluid escape pipes in sedimentary basins:
374 Implications for pipe genesis. Marine and Petroleum Geology, 65, 126–140, doi:
375 10.1016/j.marpetgeo.2015.03.023.
376 Chappell J., Shackleton N. J. (1986) Oxygen isotopes and sea level. Nature, 324, 137–140.
377 doi:10.1038/324137a0
378 Deckelman J., Connors F., Shultz A., Glagola P., Menard W., Schwegal S.- ConocoPhillips Company;
379 Shearer, J.- Applied Petrologic Technology. (2005) An Integrated Characterization of Neogene Oil and
380 Gas Reservoirs, Progreso Basin, Offshore Ecuador & Peru: Implications for Petroleum Exploration and
381 Exploitation. Perupetro S.A. INGEPET 2005.
382 Field M. E., Kvenvolden K. A. (1985) Gas hydrates on the northern California continental margin. Geology,
383 13, 517–520. doi:10.1130/0091-7613(1985)13<517:GHOTNC>2.0.CO;2
384 Fleming K., Johnston P., Zwartz D., Yokoyama Y., Lambeck K., Chappell J. (1998) Refining the eustatic
385 sea-level curve since the Last Glacial Maximum using far- and intermediate-field sites. Earth and
386 Planetary Science Letters 163, 327–342. doi: 10.1016/S0012-821X(98)00198-8
387 Foucher J.-P., Nouzé H., Henry P. (2002) Observation and tentative interpretation of a double BSR on the
388 Nankai slope. Marine Geology, 187, 161–175. doi: 10.1016/S0025-3227(02)00264-5

389 Heggland R. (1998) Gas seepage as an indicator of deeper prospective reservoirs. A study based on
390 exploration 3D seismic data. Marine and Petroleum Geology 15, 1-9. doi:10.1016/S0264-
391 8172(97)00060-3
392 Herbozo G., Hübscher C., Kaul N., Wagner M., Pecher I., Kukowski N. (2013) Influence of recent
393 depositional and tectonic controls on marine gas hydrates in Trujillo Basin, Peru Margin. Marine
394 Geology, 340, 30–48. doi: 10.1016/j.margeo.2013.04.010
395 Hübscher C., Kukowski N. (2003) Complex BSR pattern in the Yaquina Basin off Peru. Geo-Mar Lett, 23,
396 91–101. doi:10.1007/s00367-003-0128-z
397 Hustoft S., Bünz S., Mienert J., Chand S. (2009) Gas hydrate reservoir and active methane-venting
398 province in sediments on <20 Ma young oceanic crust in the Fram Strait, offshore NW-Svalbard. Earth
399 and Planetary Science Letters. doi:10.1016/j.epsl.2009.03.038.
400 Hyndman R. D., Davis E. E. (1992) A mechanism for the formation of methane hydrate and seafloor
401 bottom-simulating reflectors by vertical fluid expulsion. Journal of Geophysical Research: Solid Earth,
402 97(B5), 7025–7041. doi: 10.1029/91JB03061
403 Hyndman R. D., Foucher J. P., Yamano M., Fisher A., Scientific Team of Ocean Drilling Program Leg 131.
404 (1992) Deep sea bottom-simulating-reflectors: calibration of the base of the hydrate stability field as used
405 for heat flow estimates. Earth and Planetary Science Letters, 109, 289-301. doi: 10.1016/0012-
406 821X(92)90093-B
407 Judd A. G., Hovland M. (2009) Seabed fluid flow: the impact on geology, biology and the marine
408 environment. Cambridge University Press.
409 Koutavas, A., de Menocal P. B., Olive G. C., and Lynch-Stieglitz J. (2006), Mid-Holocene El Niño–
410 Southern Oscillation (ENSO) attenuation revealed by individual foraminifera in eastern tropical Pacific
411 sediments. Geology, 34(12), 993–996, doi:10.1130/g22810a.1
412 Kvenvolden K. A., Kastner M. (1990) Gas hydrates of the peruvian outer continental margin. Proceedings
413 of the Ocean Drilling Program, Scientific Results, 112.
414 Kvenvolden K. A. (1993) Gas hydrates—geological perspective and global change. Reviews of
415 Geophysics, 31, 173–187. doi: 10.1029/93RG00268

Lin C-.C., Lin A.T.-S., Liu C.-S., Chen G.-Y., Liao W.-Z., Schnurle P. (2008) Geological controls on BSR occurrences in the incipient arc-continent collision zone off southwest Taiwan. Marine and Petroleum Geology, 26, 1118–1131. doi: 10.1016/j.marpetgeo.2008.11.002

Milkov A. V. (2004) Global estimates of hydrate-bound gas in marine sediments: how much is really out there? Earth-Science Reviews, 66, 183–197. doi: 10.1016/j.earscirev.2003.11.002

Mitchum R. M., Vail P. R., Sangree J. B. (1977) Stratigraphic interpretation of seismic reflection patterns in depositional sequences, Part 6: in C. E. Payton, ed., Seismic Stratigraphy: Application to Hydrocarbon Exploration, 8th ed., 117–133, Am. Assoc. of Pet. Geol., Tulsa, Okla.

Mosher D. C. (2008) Bottom Simulating Reflectors on Canada's East Coast Margin: Evidence for Gas Hydrate. Proceedings of the 6th International Conference on Gas Hydrates, Vancouver, British Columbia, CANADA, July 6-10.

Paull, C.K., Ussler Iii W., Holbrook W.S., Hill T.M., Keaten R., Mienert J., Haflidason H., Johnson J.E., Winters W.J., Lorenson T.D. (2008), Origin of pockmarks and chimney structures on the flanks of the Storegga Slide, offshore Norway. Geo-Marine Letters, 28(1), 43–51, doi: 10.1007/s00367-007-0088-9

Pecher I. A., Kukowski N., Huebscher C., Greinert J., Bialas J., the GEOPECO Working Group. (2001) The link between bottom-simulating reflections and methane flux into the gas hydrate stability zone – new evidence from Lima Basin, Peru Margin. Earth and Planetary Science Letters, 185, 343–354. doi:10.1016/S0012-821X(00)00376-9

Popescu I., De Batist M., Lericolais G., Nouzé H., Poort J., Panin N., Versteeg W., Gillet H. (2006) Multiple bottom-simulating reflections in the Black Sea: Potential proxies of past climate conditions. Marine Geology, 227, 163–176. doi: 10.1016/j.margeo.2005.12.006

Posewang J., Mienert J. (1999) The enigma of double BSRs: Indicators for changes in the hydrate stability field? Geo Mar. Lett., 19, 157–163. doi: 10.1007/s003670050103

Rodrigo C., Vera E., González-Fernández A. (2009) Seismic analysis and distribution of a bottom-simulating reflector (BSR) in the Chilean margin offshore of Valdivia (40° S). Journal of South American Earth Sciences 27, 1–10. doi: 10.1016/j.jsames.2008.11.001

442 Shipley T. H., Houston M. H., Buffler R. T., Shaub F. J., McMillen K. J., Ladd J. W., Worzel J. L. (1979)
443 Seismic evidence for widespread possible gas hydrate horizons on continental slopes and rises. AAPG
444 bulletin, 63, 2204–2213.
445 Sloan E. D. (1998) Clathrate Hydrates of Natural Gases, second ed. Marcel Dekker Inc., New York &
446 Basel, 705 pp.
447 Sultan N., Cochonat P., Foucher J. P., Mienert J. (2004) Effect of gas hydrates melting on seafloor slope
448 instability. Marine Geology, 213, 379–401. doi: 10.1016/j.margeo.2004.10.015
449 Tréhu A. M., Ruppel C., Holland M., Dickens G. R., Torres M. E., Collett T. S., Goldberg D., Riedel M.,
450 Schultheiss P. (2006) Gas hydrates in marine sediments – Lessons from scientific ocean drilling.
451 Oceanography, 19, no. 4, 124–142.
452 Vanneste M., De Batist M., Golmshtok A., Kremlev A., Versteeg W. (2001) Multi- frequency seismic study
453 of gas hydrate-bearing sediments in Lake Baikal, Siberia. Marine Geology, 172, 1–21. Doi:
454 10.1016/S0025-3227(00)00117-1
455 Vanneste M., Poort J., De Batist M., Klerkx J. (2003) Atypical heat-flow near gas hydrate irregularities and
456 cold seeps in the Baikal Rift Zone. Marine and Petroleum Geology, 19, 1257–1274. doi: 10.1016/S0264-
457 8172(03)00019-9
458 von Huene R., Suess E., Emeis K. C. (1987) Convergent tectonics and coastal upwelling: a history of the
459 Peru continental margin. Episodes, 10, 87–93.
460 von Huene R., Pecher I. A. (1999) Vertical tectonics and the origins of BSRs along the Peru margin. Earth
461 and Planetary Science Letters, 166, no.1, 47–55. doi: 10.1016/S0012-821X(98)00274-X
462 Waelbroeck C., Labeyrie L., Michel E., Duplessy J. C., McManus J. F., Lambeck K., Balbon E.,
463 Labracherie M. (2002) Sea-level and deep water temperature changes derived from benthic foraminifera
464 isotopic records. Quat. Sci. Rev., 21, 295–305. doi: 10.1016/S0277-3791(01)00101-9
465 Witt C., Bourgois J. (2010) Forearc basin formation in the tectonic wake of a collision-driven, coastwise
466 migrating crustal block: The example of the North Andean block and the extensional Gulf of Guayaquil-
467 Tumbes Basin (Ecuador-Peru border area). Geological Society of America Bulletin, 122, 89–108. doi:
468 10.1130/B26386.1

Yamano M., Uyeda S., Aoki Y., Shipley T. H. (1982). Estimates of heat flow derived from gas hydrates. Geology, 10, 339–343. doi: 10.1130/0091-7613(1982)10<339:EOHFDF>2.0.CO;2

Figure captions and tables

Figure 1: (A) Location map of the main sedimentary basins along the Peruvian margin. The red box is the study area covered by seismic reflection data. The red dots mark the scientific boreholes from ODP Leg 112. The black dot marks the location of core V19-30 (Koutavas, *et al.*, 2006). (B) Bathymetric map of the study area in the Tumbes Basin. Banco Peru, a flat shallow-depth bathymetric high, marks the NW limit of the basin. The 3D seismic survey is represented by the black dashed line; the similarity attribute at seafloor reflection is highlighting discontinuities such as faults. The location of seismic figures illustrating bottom-simulating reflectors (BSRs) is represented by black straight lines. The red dashed box shows the Mancora Basin sub area in the 3D seismic block (Figures 5 and 6). (C) SW-ENE transect of the basin using 2D and 3D seismic profiles showing the main tectonic features. (D) 2D seismic profile illustrating the BSR in the SW of the Mancora Basin.

Figure 2: (A) Uninterpreted and interpreted line showing examples of DHIs in the intra-slope Mancora Basin. Seismic reflections of high amplitudes are present close to the depth of the BSR. Three horizons (H1, H2, H3) have been picked at different depths in order to intersect the BSR, and differentiate high amplitude anomalies (HAA) due to sedimentary or structural elements from those due to the BSR. The profile shows a singular HAA located beneath the BSR (yellow triangle) identified as a flat spot in NW-SE oriented profiles. (B) Example of DHIs revealing the presence of a BSR indicated by black triangles, dim out and phase reversal on a sedimentary layer of high amplitude intersected by a BSR, free gas bearing sedimentary layer of high amplitude ending onto a BSR, and seismic chimney rooted at the BSR depth. See Figure 1B for location.

Figure 3: Reflection seismic lines from the combined 2D and 3D seismic dataset showing evidence of BSRs, and multiple BSRs (intermediate and lower BSRs). See Figure 1B for location.

Figure 4: (A) Time structure map below seafloor of the distribution of the BSR, and (B) multiple BSRs. Seafloor time contours are labelled for reference. (C and D) Multiple BSRs stacking details, see Figure 3A.

Figure 5: Similarity attribute map of the seafloor highlighting the location of chimneys at the seafloor (red), and buried chimneys (yellow). Seismic chimneys ending with mounds or pockmarks at the present day seafloor (α and β), and buried chimneys ending with an intra-sedimentary doming (γ) or a patch of HAA (δ).

Figure 6: Blended TWT-structure and similarity maps of the seafloor (A) and three horizons (H1, H2, H3) (B, C, D) showing the relationship between faults azimuth and chimneys, the rose diagrams indicating the normal fault trend. The deepest horizon evidenced the highest fault density of the Mancora Basin.

Figure 7: Results from a detailed analysis of the base of the gas hydrate stability zone (GHSZ) within the 2D seismic dataset. (A) Water depth map assuming 1500 m/s seawater velocity; (B) Gas hydrate stability zone thickness assuming 1800 m/s sediment velocity; (C) Geothermal gradient computed across the mapped BSR. Contours interval is 200 m.

Figure 8: Stability conditions for gas hydrate from depth-temperature readings within the study area. Seawater temperature data compiled from World Ocean Database 2009. The theoretical curves are calculated for seawater-methane approximation with different gas compositions using the program CSMHYD of Sloan (1998).

Figure 9: Plots of observed upper BSR (black line), intermediate BSR (blue line), and lower BSR (yellow line), and computed positions of the upper BSR for present and glacial temperature and pressure conditions. See Figure 3 for original seismic observation of the BSRs.

Figure 10: Diagram showing how tectonic subsidence and sedimentation influence the depth and shape of the BSR in Figure 2A. (A) Initial state; (B) Listric normal fault developement and downward shift of the BSR; (C) Sedimentation and fault reactivation. Dissociation of hydrates (BSR) near the contact with the foot wall; (D) Sedimentation without faults reactivation. Free gas accumulation near the listric fault plane.

Table 1: Scenario of base of hydrate stability zone below seafloor for given water depths, different gas composition, and geothermal gradient. Observed BSRs depth is from the Tumbes Basin.

Water depth (m)		765			950			1115			1330		
Seafloor temperature (°C)		5.8			4.8			4.2			3.4		
Gas composition		100% CH4	96% CH4	90% CH4	100% CH4	96% CH4	90% CH4	100% CH4	96% CH4	90% CH4	100% CH4	96% CH4	90% CH4
Predicted GHSZ	geotherm 25°C/km	245	425	615	390	530	680	475	585	725	550	645	780
thickness (m)	geotherm 40°C/km	125	235	245	215	300	410	250	325	420	300	360	445
Observed BSR	upper BSR	225			306			432			441		
depth (mbsf)	lower BSR	351			414			567			540		

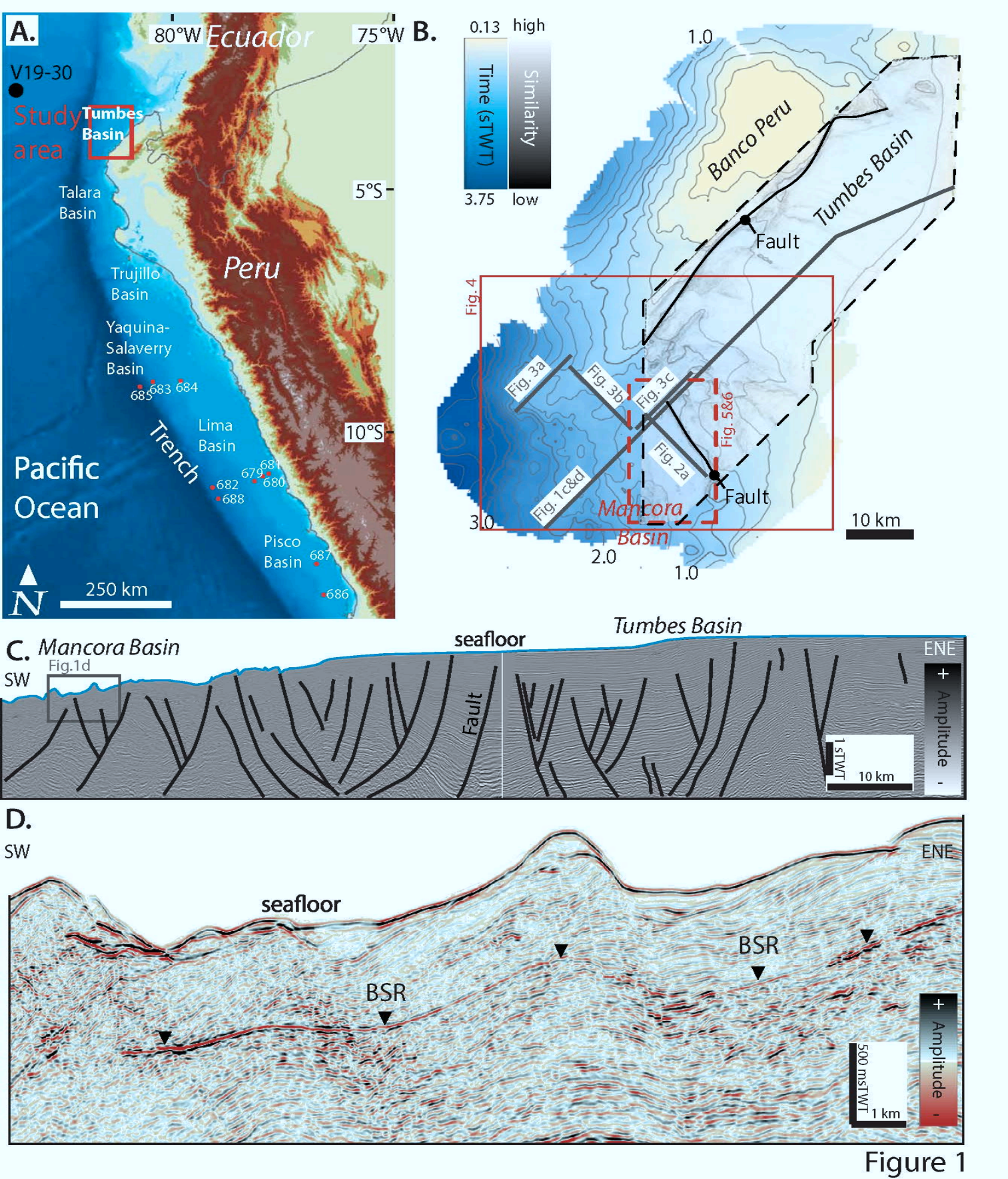
A.
80°W
Ecuador
75°W
V19-30
Study area
Tumbes Basin
Talara Basin
5°S
Peru
Trujillo Basin
Yaquina-Salaverry Basin
685
683
684
Lima Basin
10°S
Trench
Pacific Ocean
679
681
680
682
688
Pisco Basin
687
686
N
250 km
B.
0.13
high
Time (sTWT)
Similarity
3.75
low
1.0
Banco Peru
Tumbes Basin
Fault
Fig. 4
Fig. 3a
Fig. 3b
Fig. 3c
Fig. 5&6
Fig. 2a
Fig. 1c&d
Fault
Mancora Basin
3.0
2.0
1.0
10 km
C.
Mancora Basin
Fig.1d
SW
seafloor
Tumbes Basin
ENE
Fault
+
Amplitude
-
1 sTWT
10 km
D.
SW
ENE
seafloor
BSR
BSR
+
Amplitude
-
500 msTWT
1 km

Figure 1

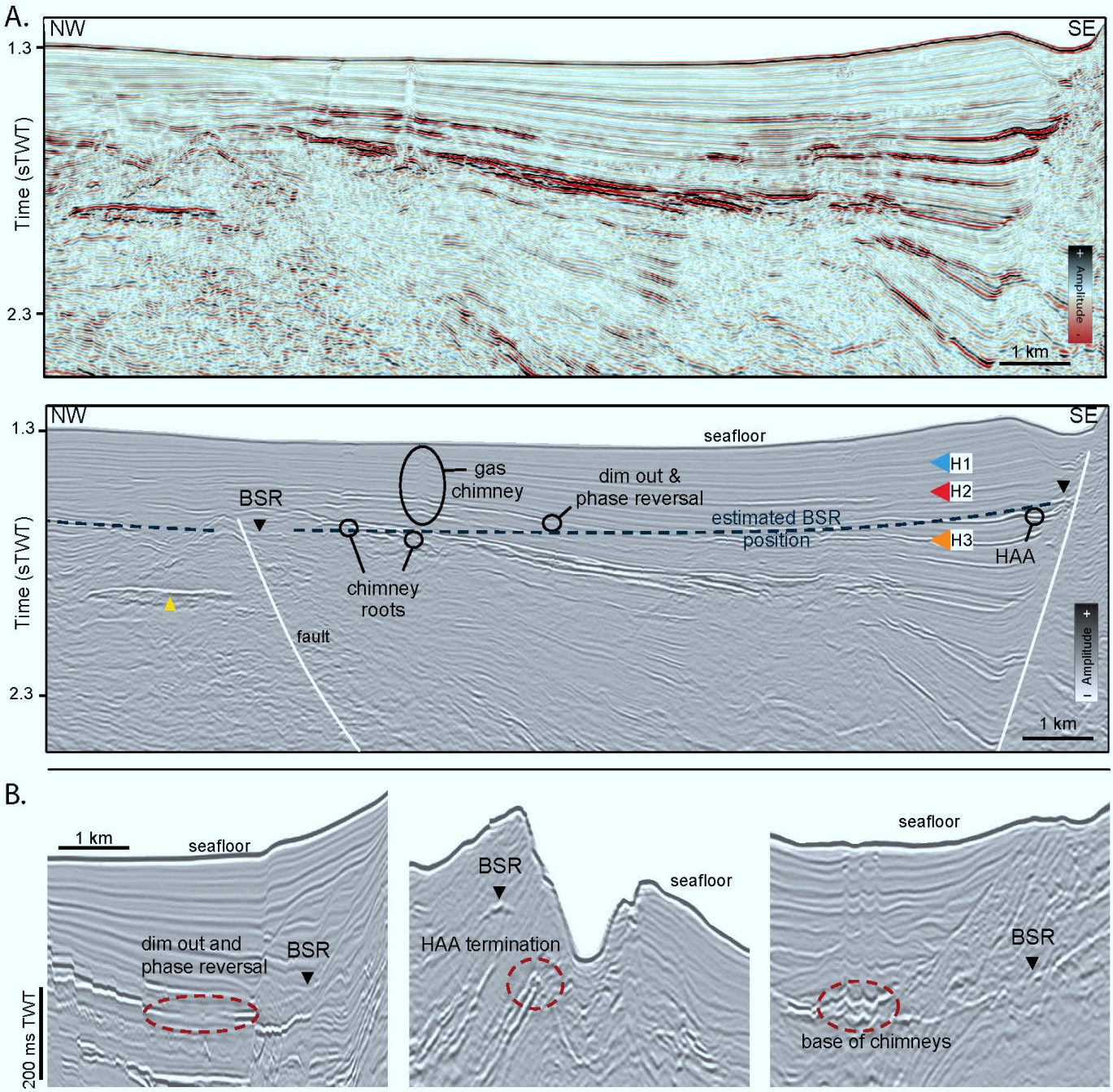
A.
NW
SE
1.3
2.3
Time (sTWT)
+ Amplitude -
1 km
NW
SE
1.3
2.3
Time (sTWT)
seafloor
gas chimney
dim out & phase reversal
BSR
estimated BSR position
H1
H2
H3
HAA
chimney roots
fault
+ Amplitude -
1 km
B.
1 km
seafloor
dim out and phase reversal
BSR
200 ms TWT
BSR
seafloor
HAA termination
seafloor
BSR
base of chimneys

Figure 2

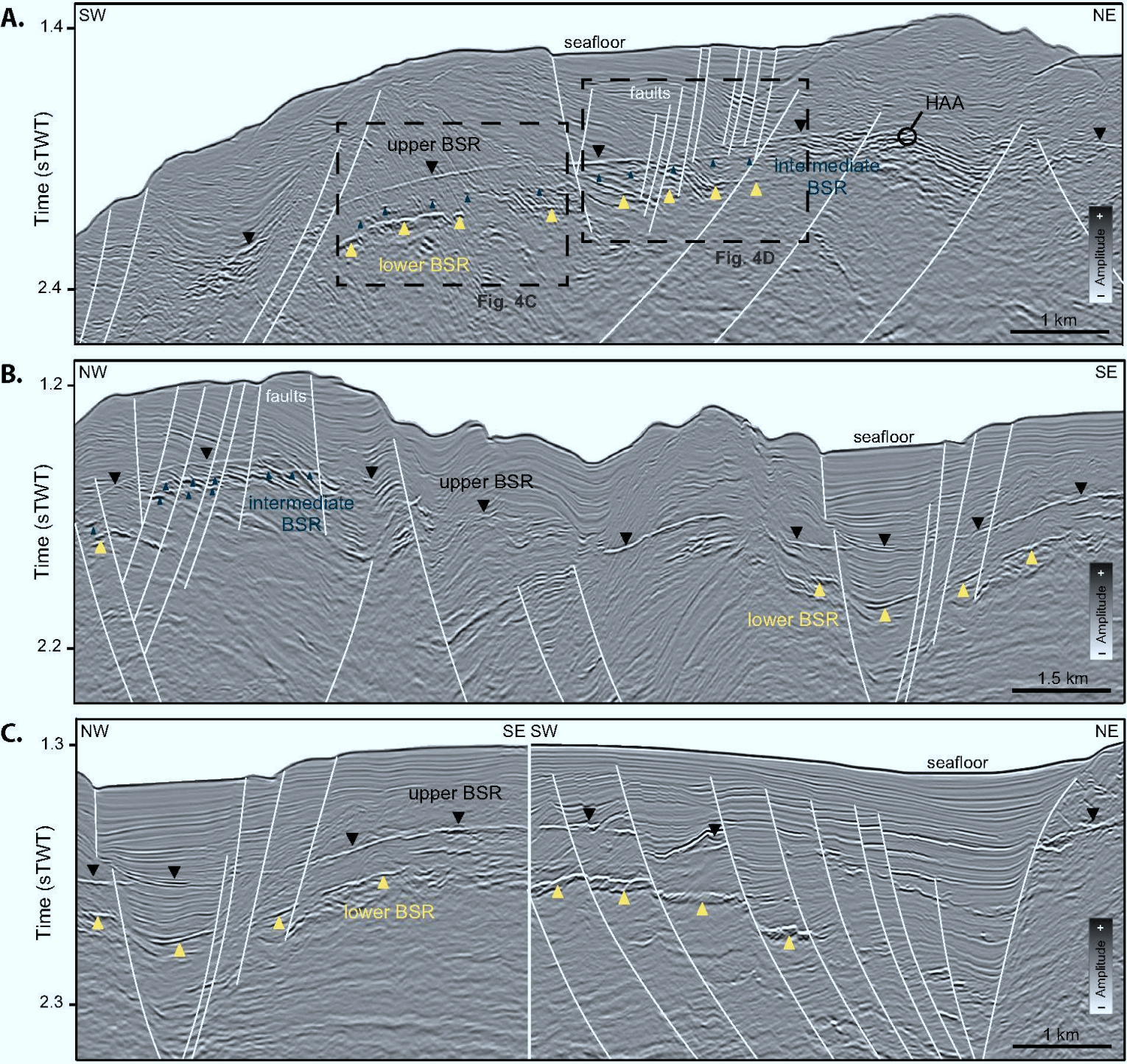
A.
SW
NE
1.4
2.4
Time (sTWT)
seafloor
faults
HAA
upper BSR
intermediate BSR
lower BSR
Fig. 4C
Fig. 4D
+ Amplitude -
1 km
B.
NW
SE
1.2
2.2
Time (sTWT)
faults
seafloor
upper BSR
intermediate BSR
lower BSR
+ Amplitude -
1.5 km
C.
NW
SE SW
NE
1.3
2.3
Time (sTWT)
upper BSR
lower BSR
seafloor
+ Amplitude -
1 km

Figure 3

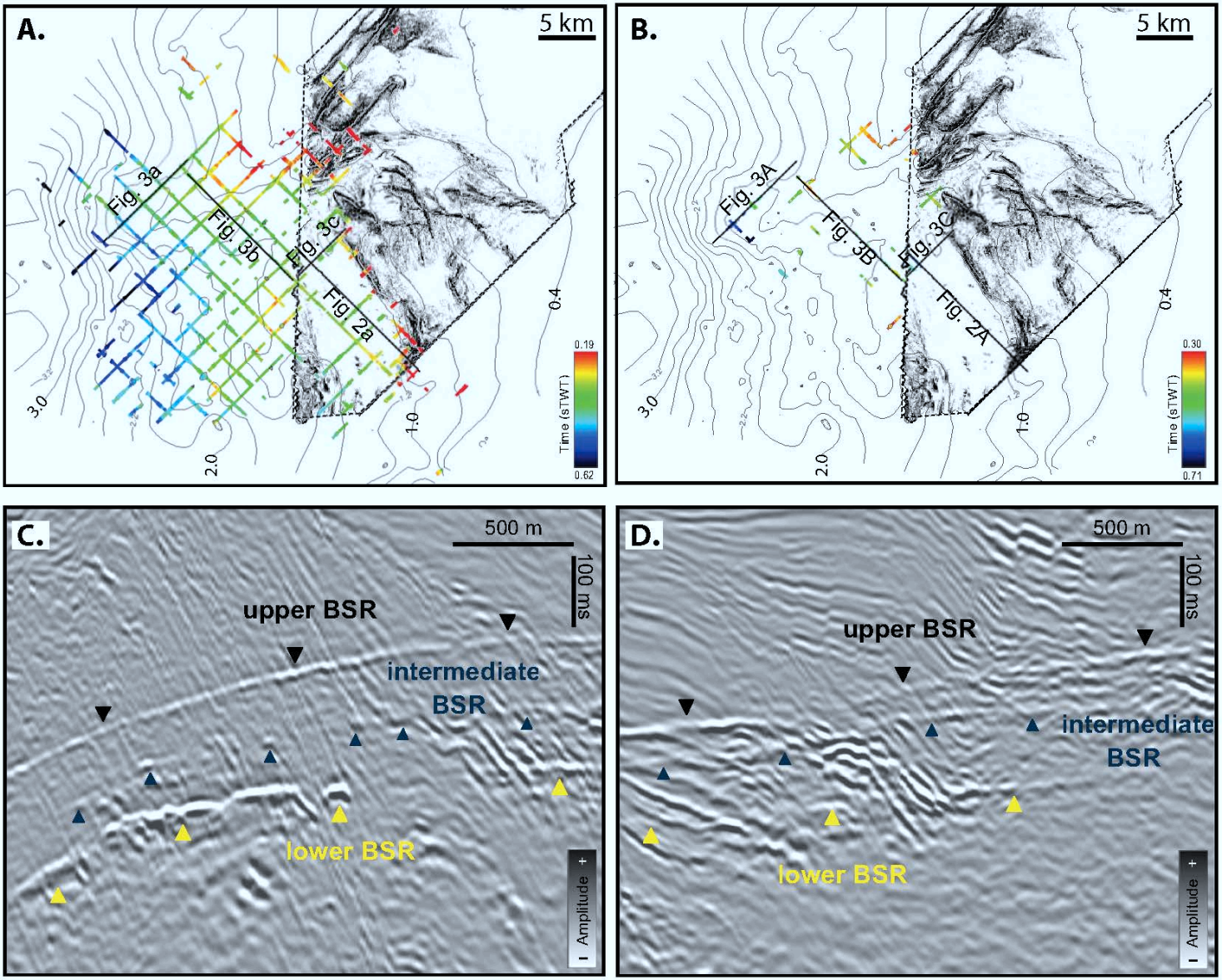
A.
5 km
Fig. 3a
Fig. 3b
Fig. 3c
Fig. 2a
3.0
2.0
1.0
0.4
0.19
Time (sTWT)
0.62
B.
5 km
Fig. 3A
Fig. 3B
Fig. 3C
Fig. 2A
3.0
2.0
1.0
0.4
0.30
Time (sTWT)
0.71
C.
500 m
100 ms
upper BSR
intermediate BSR
lower BSR
Amplitude + -
D.
500 m
100 ms
upper BSR
intermediate BSR
lower BSR
Amplitude + -

Figure 4

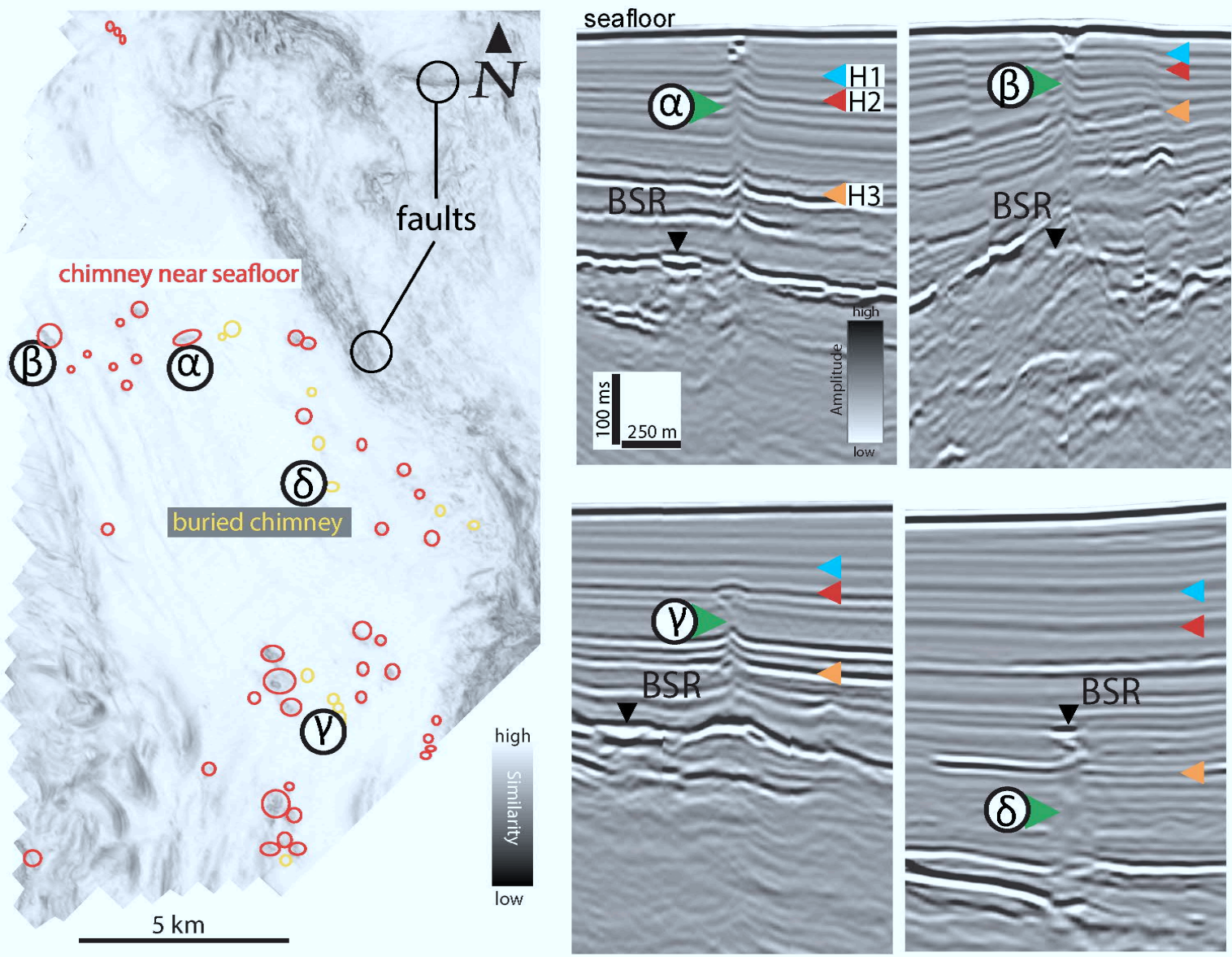
N
faults
chimney near seafloor
β
α
δ
buried chimney
γ
high
Similarity
low
5 km
seafloor
H1
H2
H3
BSR
high
Amplitude
low
100 ms
250 m
β
BSR
γ
BSR
BSR
δ

Figure 5

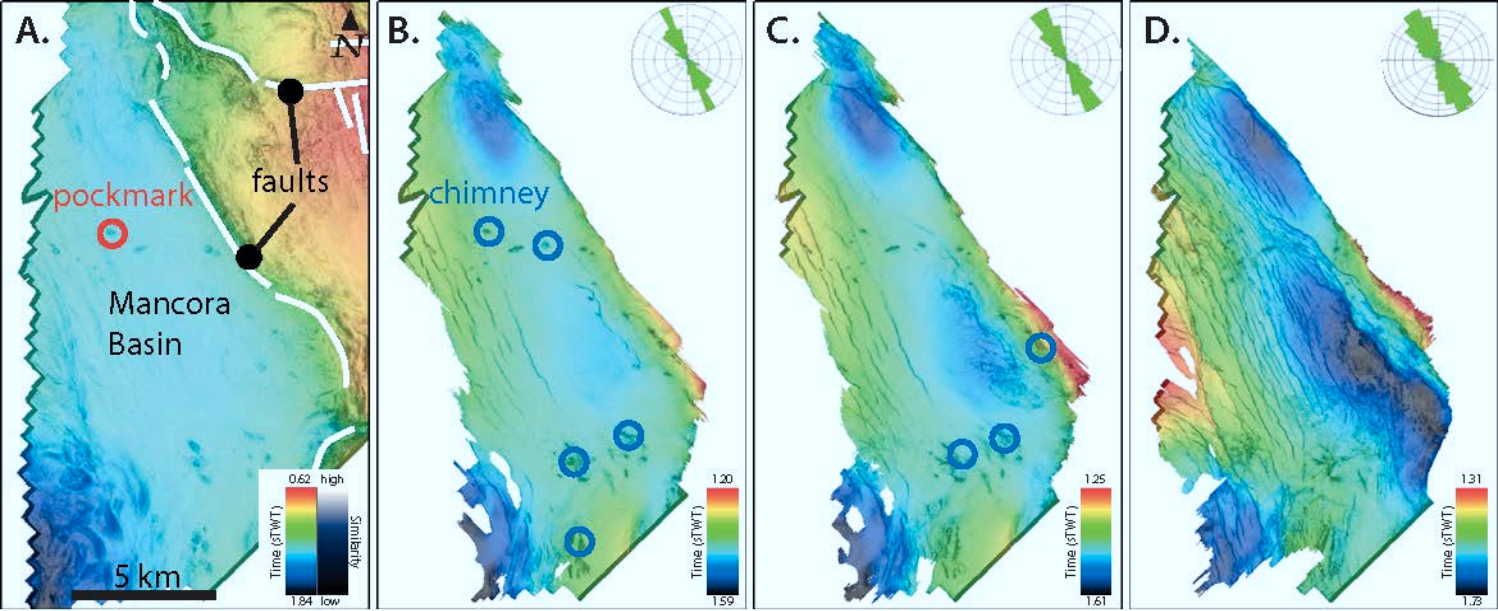
A.
N
pockmark
faults
Mancora
Basin
0.62 high
Time (sTWT)
Similarity
1.84 low
5 km
B.
chimney
1.20
Time (sTWT)
1.59
C.
1.25
Time (sTWT)
1.61
D.
1.31
Time (sTWT)
1.73

Figure 6

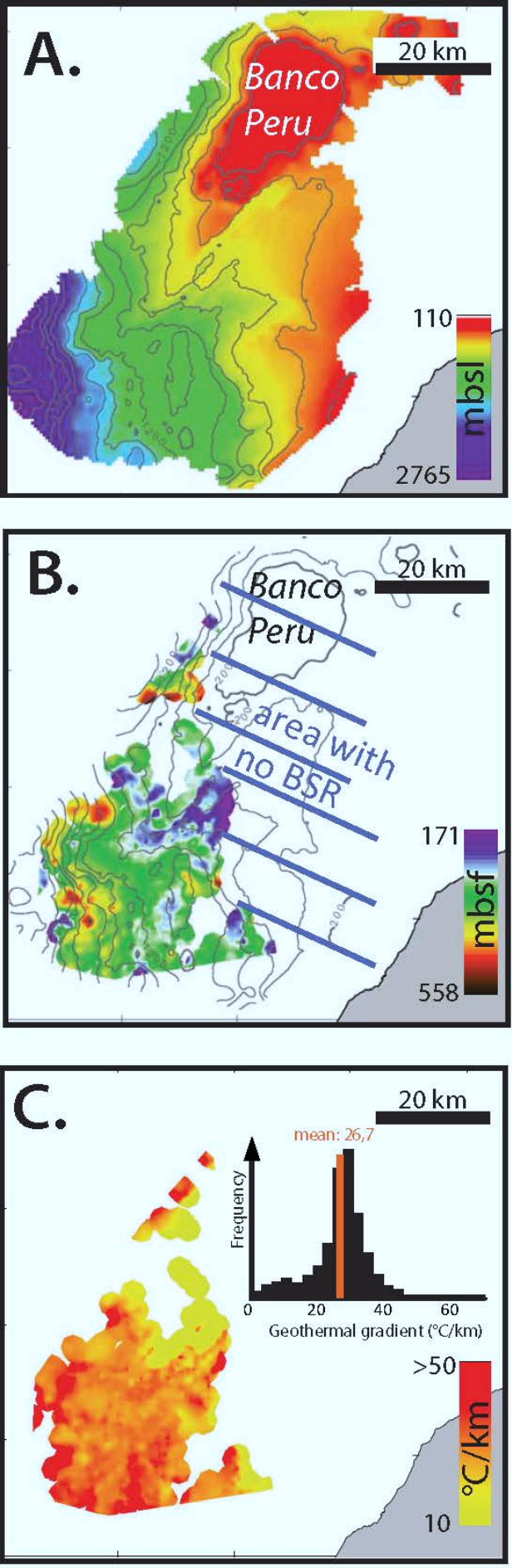
A.
20 km
Banco
Peru
110
mbsl
2765
B.
20 km
Banco
Peru
area with
no BSR
171
mbsf
558
C.
20 km
mean: 26,7
Frequency
0
20
40
60
Geothermal gradient (°C/km)
>50
°C/km
10

Figure 7

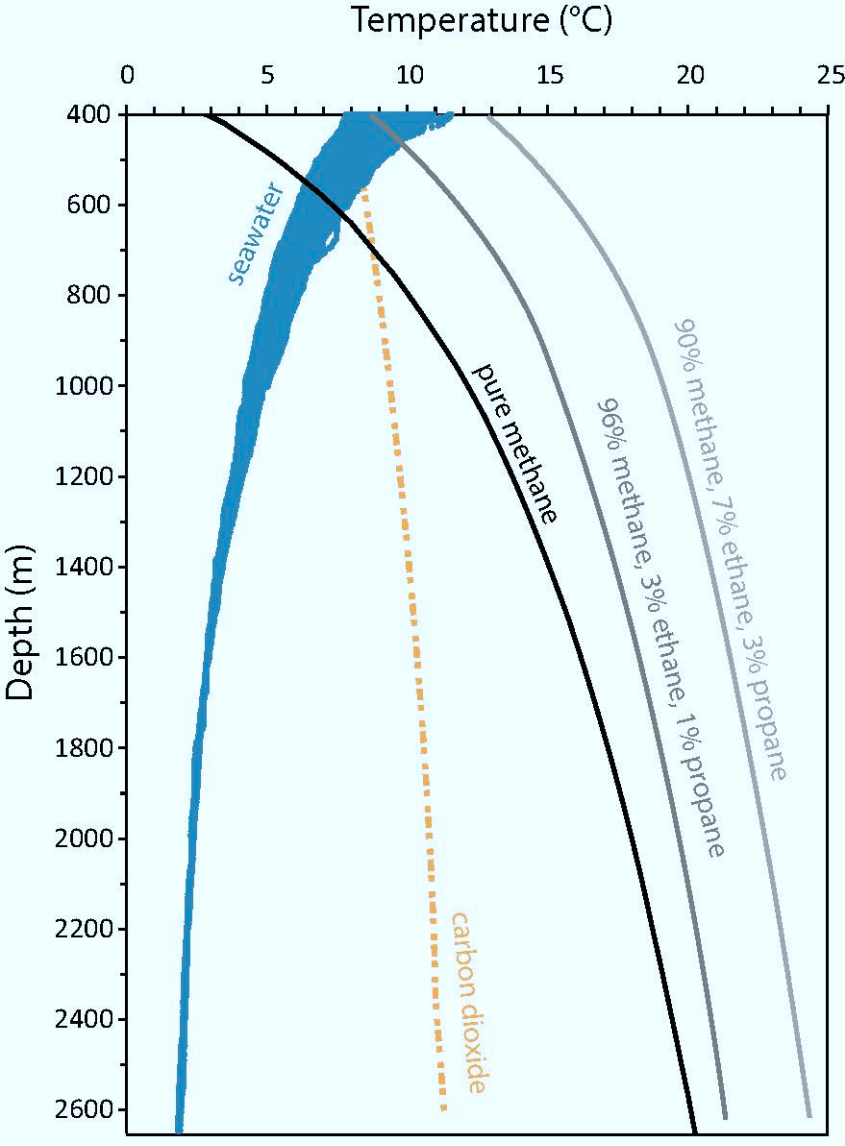
Temperature (°C)
0
5
10
15
20
25
Depth (m)
400
600
800
1000
1200
1400
1600
1800
2000
2200
2400
2600
seawater
pure methane
96% methane, 3% ethane, 1% propane
90% methane, 7% ethane, 3% propane
carbon dioxide

Figure 8

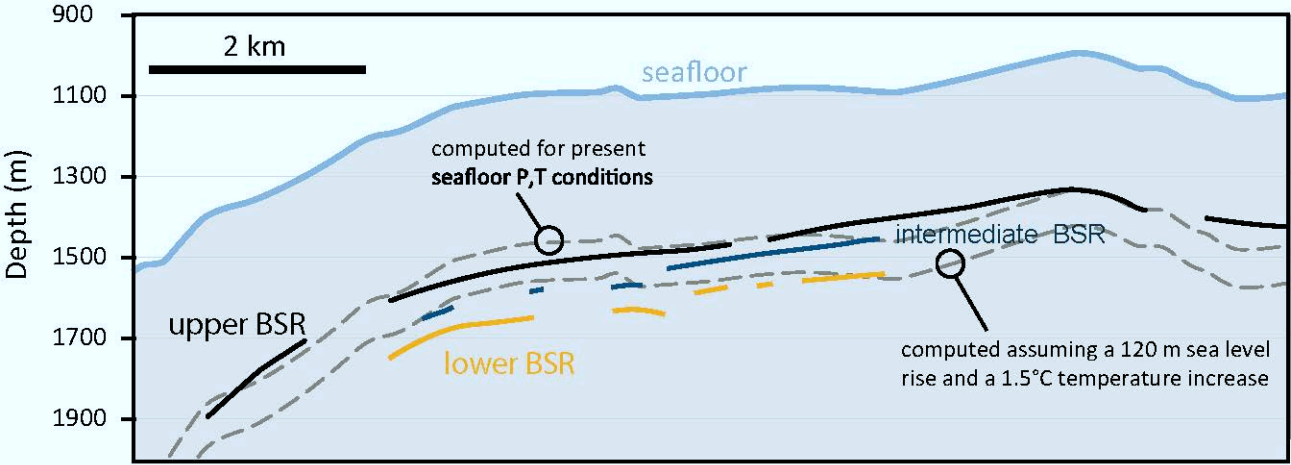
900
1100
1300
1500
1700
1900
Depth (m)
2 km
seafloor
computed for present
seafloor P,T conditions
intermediate BSR
upper BSR
lower BSR
computed assuming a 120 m sea level
rise and a 1.5°C temperature increase

Figure 9

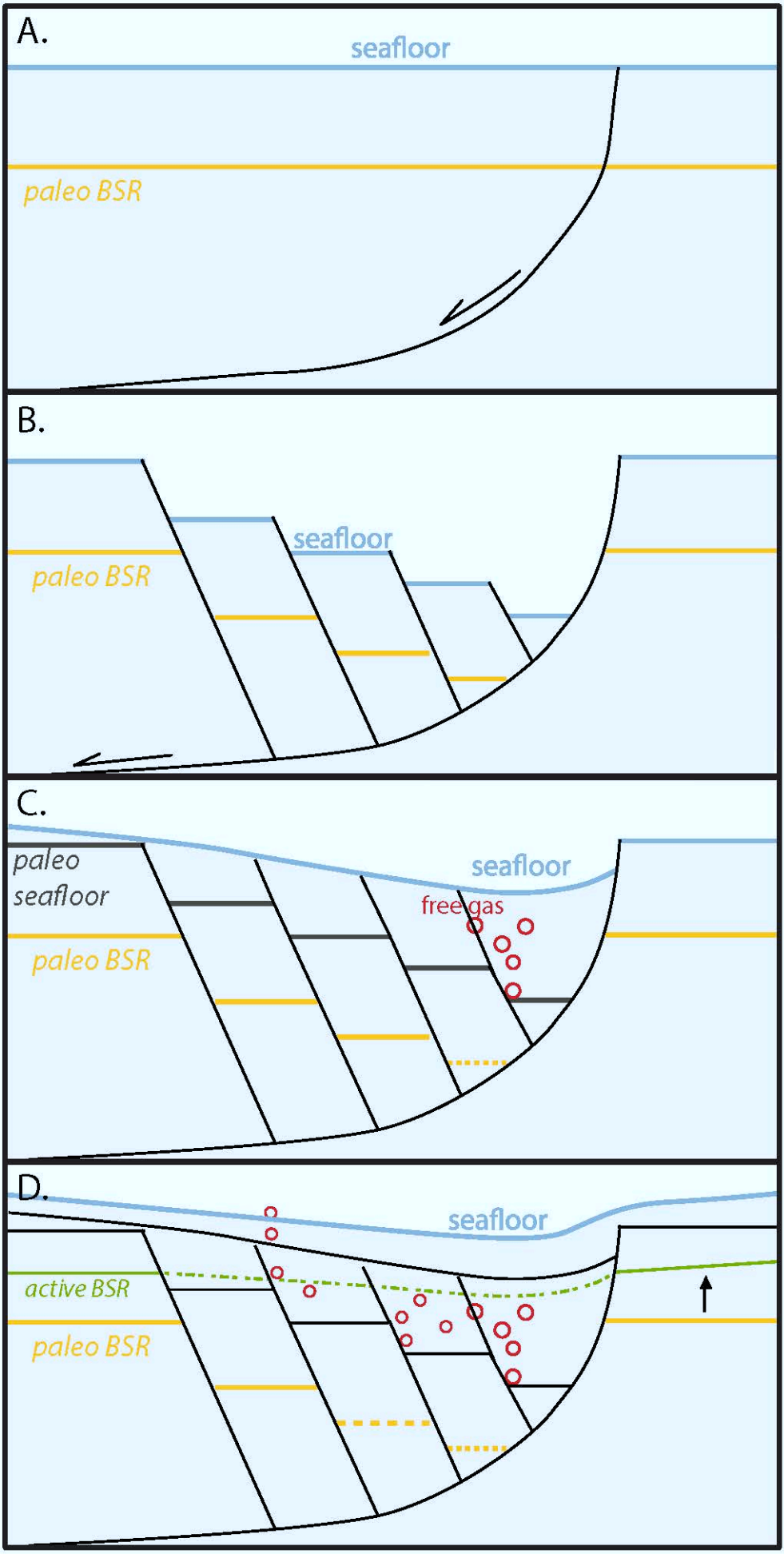
A.
seafloor
paleo BSR
B.
seafloor
paleo BSR
C.
paleo
seafloor
seafloor
free gas
paleo BSR
D.
seafloor
active BSR
paleo BSR

Figure 10